ACS OMEGA

http://pubs.acs.org/journal/acsodf

Article

MIL-100(Fe)-Hybridized Nanofibers for Adsorption and Visible Light Photocatalytic Degradation of Water Pollutants: Experimental and DFT Approach

Halim Lee, Hyungwoo Lee, Soyeon Ahn, and Jooyoun Kim*

Cite This: *ACS Omega* 2022, 7, 21145−21155

Read Online

ACCESS | Metrics & More | Article Recommendations | Supporting Information

ABSTRACT: As rapid industrial growth spawns severe water contamination and a far-reaching impact on environmental safety, the development of a purification system is in high demand. Herein, a visible light-induced photocatalytic adsorbent membrane was developed by growing a porous metal−organic framework (MOF), MIL-100(Fe) crystals, onto electrospun polyacrylonitrile (PAN) nanofibers, and its purification capability by adsorption and the photocatalytic effect was investigated. As water-soluble organic foulants, a cationic dye, rhodamine B (RhB), and an anionic dye, methyl orange (MO), were employed, and the adsorption/desorption characteristics were analyzed. Since MIL-100(Fe) possesses positive charges in aqueous solution, MO was more rapidly adsorbed onto the MIL-100(Fe) grown PAN membrane (MIL-100(Fe)@PAN) than RhB. Under visible light, both photocatalytic degradation and adsorption occurred concurrently, facilitating the purification process. The reusability of MIL-100(Fe)@PAN as an adsorbent was explored by cyclic adsorption−desorption experiments. Density functional theory (DFT) calculations corroborated higher binding energy of charged MO over RhB and demonstrated the possible steric hindrance of RhB to adhere in MOF pores. The emphasis of the study lies in the combined investigation of the experimental approach and DFT calculations for the fundamental understanding of adsorption/desorption phenomena occurring in the purification process. This study provides theoretical support for the interaction between MOF−hybrid complexes and contaminants when MOF-hybridized composites adsorb or photodegrade water-soluble pollutants of different charges and sizes.

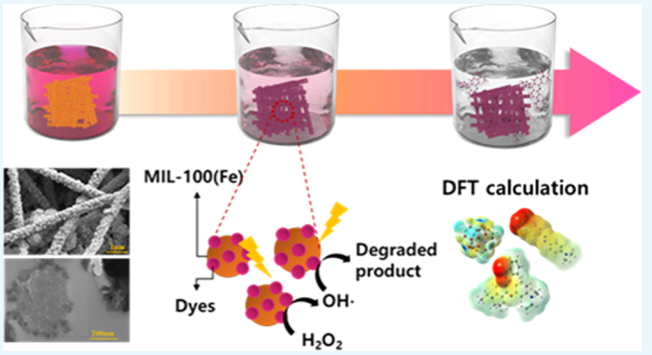

1. INTRODUCTION

Industrial and daily chemicals produced from dyes, detergents, pharmaceuticals, and personal care products cause severe water contamination, posing a serious threat to public health.[1] As water use increases rapidly and clean water becomes scarce, it is of great interest to properly treat and recycle wastewater. In this regard, the development of effective water purification technology is in high demand. Among various wastewater treatment methods, adsorption is one of the most convenient and effective strategies for removing organic pollutants in wastewater.[2,3] Porous materials such as activated carbon and zeolite are used as common adsorbents with their high porosity and surface area.[4] In this method, the used adsorbents are to be disposed of as hazardous waste when the adsorption site is saturated with adsorbates. Another purification strategy is to employ photocatalytic degradation,[5] in which a photocatalyst is excited by the light-induced energy higher than its band gap to generate electrons and holes. These electron−hole pairs produce reactive oxygen species (ROS) that drive redox reactions to decompose pollutants. Photocatalysts such as titanium dioxide and zinc oxide are commonly used as effective photocatalysts, but these photocatalysts require UV irradiation to overcome the band gap, restraining the effective redox process under visible light.[6,7] Nonetheless, photocatalytic degradation is considered an efficient decontamination strategy beyond the limitation of adsorption capacity.[8]

Rather recently, metal−organic frameworks (MOFs), composed of metal clusters and organic linkers, have drawn great attention as next-generation adsorbents with a highly porous structure and the semiconductor-like behavior that leads to photocatalysis.[9,10] MOFs produce ROS upon light irradiation, and these ROS such as $^{\bullet}OH$, H_2O_2, and $O_2^{\bullet-}$ are responsible for the degradation of organic compounds.[11,12] In addition, the high specific surface area with a large pore volume and diversified functional groups make MOFs promising

Received: March 30, 2022
Accepted: May 31, 2022
Published: June 9, 2022

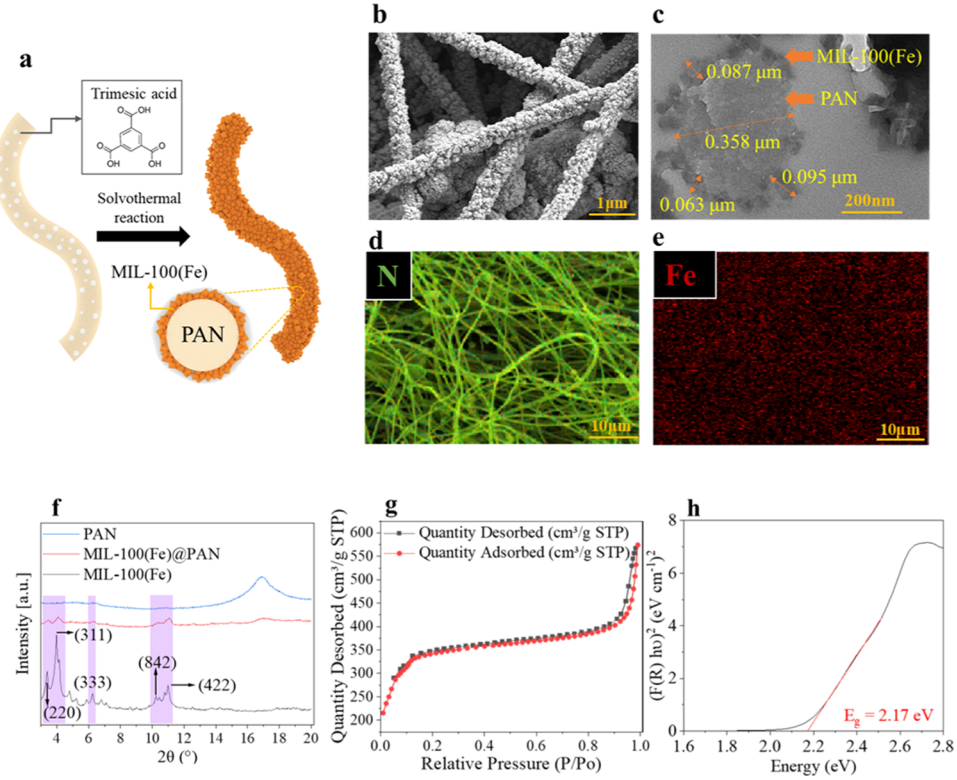

Figure 1. Characterization of MIL-100(Fe)@PAN. (a) Schematic illustration of the synthesis procedure of the MIL-100(Fe)@PAN composite. (b, c) Scanning electron microscopy (SEM) and transmission electron microscopy (TEM) images of the membrane surface and energy-dispersive spectrometry (EDS) mapping of MIL-100(Fe)@PAN with (d) nitrogen (N) and (e) iron (Fe) ions. (f) X-ray diffraction (XRD) peaks of PAN, MIL-100(Fe), and MIL-100(Fe)@PAN. (g) N_2 adsorption and desorption graphs of MIL-100(Fe). (h) Tauc plot of MIL-100(Fe).

adsorbents in many applications.[13] Among the various types of MOFs, MIL-100(Fe) is a good candidate for application in wastewater treatment, due to its low toxicity, water stability, and Fenton-like photocatalytic activity.[14−17] In particular, the low band gap energy of MIL-100(Fe), ∼2.17 eV, makes it easier to produce ROS under visible light.[18] On the other hand, a low band gap can be a disadvantage in that the produced electrons and holes can readily recombine, failing the effective generation of ROS and hindering the photocatalytic efficiency. To overcome this problem, a strong oxidant or electron acceptor, such as H_2O_2, can be used to prevent rapid recombination.[19,20] The photocatalytic ability not only allows the continuous degradation of pollutants at the MOF interface but also helps the degradation of adsorbates already captured on MOF. With the dual function of MOF as a high-capacity adsorbent and photocatalytic agent, its application in efficient wastewater treatment is highly anticipated.

To date, varied types of MOF-hybridized composites have been investigated for their applications in fields with various functions, such as gas adsorption,[21,22] sterilization,[23,24] and photocatalytic activity.[25,26] However, the research studies based on MOF-hybridized composites are mostly focused on exploring the conditions under which the maximum photodegradation and adsorption were achieved, rather than analyzing the individual contribution to the total removal capability.[26−28] Also, the findings from previous studies on the effect of environmental conditions (pH, contaminant types, etc.) on the adsorption efficiency are very useful, yet practically, we have limited control over the environmental conditions to attain the maximum efficiency. Generally, MOFs are anticipated to be selective toward charges and sizes of foulants, and the removal efficiency and rate would be dependent on the interactions based on those foulant characteristics. Thus, it seems to be fundamentally necessary to investigate the interaction between the foulants and the adsorbents for developing a practical and economical adsorbent, and this is one of the specific aims of this study. Also, we aim at evaluating the contribution of adsorption to the overall foulant removal that is attributed to both adsorption and photodegradation and assessing the effective removal mechanisms depending on the foulant types.

Herein, a MIL-100(Fe)-hybridized polyacrylonitrile (PAN) nanofiber composite membrane (MIL-100(Fe)@PAN) was fabricated to grant dual function of adsorption and visible light-driven photocatalytic activity for the efficient removal of water-soluble dyes. The adsorption capacity and kinetics of MIL-100(Fe)@PAN were investigated for both a cationic dye, rhodamine B (RhB), and an anionic dye, methyl orange (MO), and its cyclic usability was probed by the repeated adsorption/desorption experiments. In addition, molecular interactions between MOF and dyes were systemically investigated using DFT calculations. The ground-state structures, electrostatic potential, and adsorption enthalpies of the molecules were obtained considering their spin configurations. The calculated binding energy between the dye adsorbates and MIL-100(Fe) was associated with the adsorption/desorption phenomena. Also, the purification performance by the concurrent action of photodegradation and adsorption was investigated. This study employs a novel approach of combined investigation of experiments and DFT calculation, to reveal the molecular interactions between the adsorbent and adsorbate. The calculation of binding energy revealed the interactions of

https://doi.org/10.1021/acsomega.2c01953
ACS Omega 2022, 7, 21145−21155

MIL-100(Fe) and foulants at the atomic level during the adsorption/desorption processes, and the reusability experimental results were explained by the findings from the DFT analysis. This study is significant in providing an informative discussion on the contribution of adsorption and photocatalytic activity, and it intends to give a practical value in developing photocatalytic adsorbent materials.

2. EXPERIMENTAL SECTION

2.1. Materials. Trimesic acid (H_3BTC) and PAN (M_w 150,000) were purchased from Sigma-Aldrich. Iron(III) chloride hexahydrate ($FeCl_3{\cdot}6H_2O$) was obtained from Fuji, Japan. Ethanol (99.9%), *N*,*N*-dimethylformamide (DMF, 99.5%), and rhodamine B (RhB) were supplied by SCI Seoul Chemicals, Korea. Methyl orange (MO) was obtained from Daejung Chemicals, Korea. Isopropanol (IPA) and 1,4-benzoquinone (BQ) were purchased from Daejung Chemicals, Korea. Ammonium oxalate monohydrate (AO) was purchased from Junsei Chemical Co., Japan. All materials were of analytical grade and used without further treatment.

2.2. Preparation of MIL-100(Fe) Powder and MIL-100(Fe)@PAN. Hydrothermal synthesis of MIL-100(Fe) was conducted as shown in Figure 1a. PAN powder (1.0 g) was dissolved in 10 mL of DMF. Then, 0.1 g of H_3BTC was added in sequence and finally, a pre-spinning PAN solution was stirred at 70 °C for 12 h. The dynamic viscosity of the solution at the varied shear rates is given in Figure S1, and the conductivity of the solution was 110.6 μs cm^{-1}. The H_3BTC-containing pre-spinning solution was electrospun at the bias voltage of 18−19 kV and a flow rate of 1 mL h^{-1}. The solution was ejected onto a rotating drum collector wrapped with aluminum foil at 200 rpm from a distance of 15 cm. The collected electrospun composite web was dried at 60 °C for 24 h. The electrospinning process parameters were accustomed to producing bead-free nanofibers in the consistent size range for the respective fibers. Electrospinning was conducted at a temperature of 25 ± 2 °C and a relative humidity of 50 ± 3% RH.

After electrospinning PAN, MIL-100(Fe)@PAN was synthesized by hydrothermal synthesis. The dried 400−450 mg of nanofiber membrane was placed in a Teflon-lined stainless-steel autoclave with the prepared solution. The solution was mixed with 30 mmol of iron(III) chloride hexahydrate, 20 mmol of trimesic acid, and 60 mL of distilled water. The autoclave was kept at 140 °C for 14 h. When the hydrothermal process ended, the membrane was rinsed with ethanol at 60 °C for 12 h, then dried for 24 h in a vacuum oven (LVO2051P, Daihan Labtech). Pure MIL-100(Fe) powder was synthesized with the same hydrothermal process without the nanofiber membrane. The collected powder was rinsed with ethanol and distilled water several times, then kept at 60 °C for 24 h.

2.3. Characterization. The morphology of MIL-100(Fe) powder and MIL-100(Fe)@PAN was characterized by field emission scanning electron microscopy (FE-SEM, MERLIN Compact, ZEISS). The particle and fiber sizes were measured from SEM images using Image J software (NIH). The elemental composition of MIL-100(Fe)@PAN was analyzed by energy-dispersive spectroscopy (EDS, NORAN system 7, Thermo Scientific). Energy-filtering transmission electron microscopy (EF-TEM, LIBRA 120, ZEISS) was used to observe the morphology of MIL-100(Fe)@PAN. The conductivity of the pre-spinning solution was examined using a conductivity meter (HC9021, Trans Instruments) and viscosity was evaluated using a rheometer (Advanced Rheometric Expansion System, Rheometric Scientific). Chemical composition was analyzed by Fourier transform infrared (FT-IR, TENSOR27, Bruker) spectra. X-ray diffraction (XRD) analysis was performed on an X-ray diffractometer (D8 Advance, Bruker) using Cu Kα (λ = 1.540562 Å, 40 kV, 40 mA) as the X-ray source, at a scanning rate of 0.4° s^{-1} in the range from 3 to 20°. The X-ray diffraction pattern was analyzed using DIFFRAC.SUITE software. Brunauer−Emmet−Teller (BET) measurement was conducted in N_2 at 77 K (Tristar II 3020, Micromeritics). Diffuse reflectance spectra were recorded using a spectrophotometer (CM 2600d, Konica Minolta) followed by SpectraMagic NX color software. The Tauc plot was obtained from the Kubelka−Munk function, $F(R_\infty)$, following eqs 1 and 2

$$F(R_\infty) = \frac{K}{S} = \frac{(1 - R_\infty)^2}{2R_\infty} \tag{1}$$

$$(F(R_\infty){\cdot}h\nu)^{1/\gamma} = B(h\nu - E_g) \tag{2}$$

where $R_\infty = \frac{R_{sample}}{R_{standard}}$ is the reflectance of the specimen, K is the absorption coefficient, S is the scattering coefficient, h is the Plank constant, ν is the photon's frequency, E_g is the band gap energy, and B is a constant. γ depends on the nature of the electron transition and a γ value of 0.5 for the direct transition was used in this experiment.[29]

Thermogravimetric analysis (TGA, Discovery TGA, TA Instruments) was carried out under air at a heating rate of 10 °C min^{-1} up to 800 °C. The Zeta potential of MIL-100(Fe) was measured using an electrophoretic light scattering spectrophotometer (ELS Z-1000, Otsuka Portal) at pH 7. The stress−strain behavior of the sample was evaluated using a universal testing machine (model 5 ST, Tinius Olsen).

2.4. Dye Adsorption Kinetics of MIL-100(Fe)@PAN. Adsorption of RhB and MO dyes was evaluated, immersing the 3 cm × 3 cm sample of MIL-100(Fe)@PAN (mass of 0.0616 ± 0.0147 g) in 50 mL of aqueous dye solution at pH 7 with stirring. The concentration of the dye was examined by measuring the absorbance at a λ_{max} value of 553 nm for RhB and 505 nm for MO using a multi-mode microplate reader (Synergy H1, BioTek). Adsorption of RhB and MO per unit mass of MIL-100(Fe)@PAN at equilibrium, Q_e (mg g^{-1}) was obtained by eq 3

$$Q_e = \frac{(C_0 - C_e)V}{m} \tag{3}$$

where C_0 (mg L^{-1}) and C_e (mg L^{-1}) are the concentrations of the dye at the initial and the equilibrium states, respectively. V (L) is the volume of dye solution, and m (g) is the mass of MIL-100(Fe)@PAN used. All adsorption tests were performed in the dark to exclude the effect of photodegradation.

2.5. Photodegradation Performance of MIL-100(Fe)@PAN. The photocatalytic activity of the MIL-100(Fe)@PAN sample (3 cm × 3 cm) to degrade dyes was evaluated in a 50 mL of 20 mg L^{-1} aqueous dye solution. To facilitate Fenton activity, 1 mL of H_2O_2 was added to the solution and the light (F20T12/65 6500K lamp, GretagMacbeth) was turned on.[30] The solution was continuously stirred during the test for a homogeneous reaction. Three control tests were included: (1) PAN membrane under light, (2) MIL-100(Fe)@PAN under

https://doi.org/10.1021/acsomega.2c01953
ACS Omega 2022, 7, 21145−21155

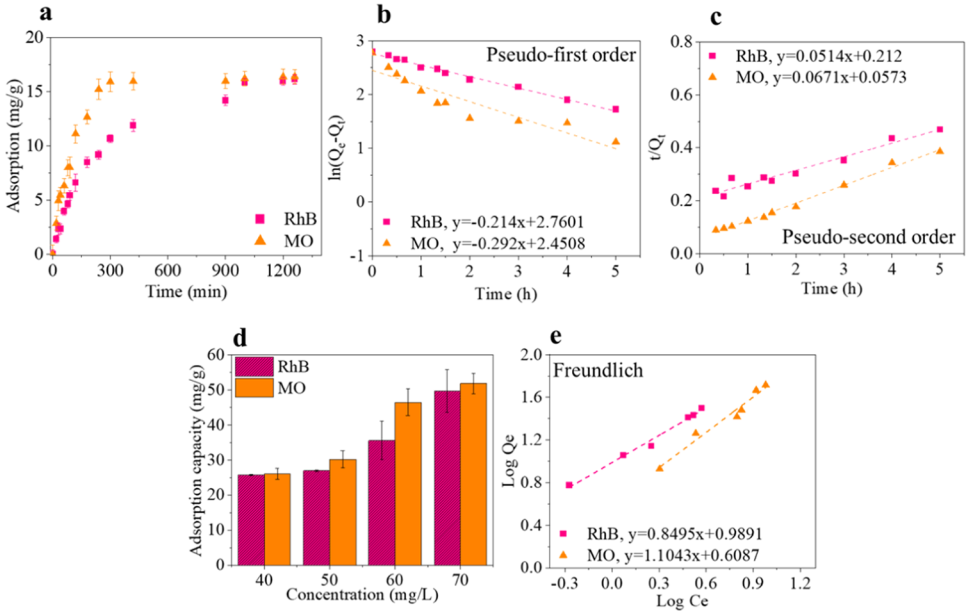

Figure 2. Adsorption kinetics and capacity of MIL-100(Fe)@PAN. (a) Adsorption of RhB and MO with time in the concentration of 20 mg L^{-1}. (b) Pseudo-first-order and (c) pseudo-second-order adsorption kinetics fitting the experimental data. (d) Dye adsorption capacities of MIL-100(Fe)@PAN under varied concentrations. (e) Linear fitting of Freundlich isotherms (initial dye concentration: 5−70 mg L^{-1}) for RhB and MO.

dark, and (3) H_2O_2 addition without membrane under light. The photocatalytic efficiency was evaluated by eq 4

$$\text{photodegradation efficiency} = \frac{C_{pt}}{C_0} \tag{4}$$

where C_0 is the initial dye concentration and C_{pt} is the dye concentrations at time t with photocatalytic reaction progressed upon light irradiation.

2.6. Recyclability of MIL-100(Fe)@PAN. After the adsorption experiment at the initial dye concentration of 5 mg L^{-1}, the MIL-100(Fe)@PAN was immersed in 50 mL of ethanol at room temperature (25 °C) and shaken in the shaking water bath (LB-SW060, LKLAB Korea) at 100 rpm for 6 h, to wash off the adsorbed dyes. Prior to the next cycle of the adsorption test, the MIL-100(Fe)@PAN sample subjected to the washing procedure was dried at 60 °C. The adsorption test was repeated in 50 mL of 5 mg L^{-1} dye solution. To examine the performance of repeated adsorptions, the adsorption and desorption cycle was repeated five times, and the adsorption efficiency was evaluated by eq 5

$$\text{adsorption efficiency} = \frac{C_t}{C_0} \tag{5}$$

$$\text{desorption efficiency (\%)} = \frac{C_{de}}{C_{ad}} \times 100 \tag{6}$$

where C_0 is the initial dye concentration and C_t is the dye concentrations at time t with the adsorption process in dark. The desorption efficiency was calculated by eq 6: where C_{de} is the desorbed dye concentration and C_{ad} is the adsorbed dye concentration.

2.7. DFT Analysis of Adsorption and Desorption. A computational study was performed using the Gaussian 09 package[31] to describe the intermolecular interaction between MIL-100(Fe) and dyes, RhB and MO. The gas-phase geometrics of all molecules were optimized based on the B3LYP exchange-correlation functional with 6-311+g(d,p) for C, O, H, Cl, S, and N atoms[32−34] and LANL3DZ basis set for the Fe atom with an effective core potential.[35,36] Binding energy (BE) at 298 K for two distinct molecules is defined by eq 7

$$\text{BE}(\Delta H) = E_{\text{MOF}} + E_{\text{dye}} - E_{\text{complex}} \tag{7}$$

where E_{MOF}, E_{dye}, and E_{complex} are the ground-state energies of MOF, dye, and their complex, respectively.

Frequency calculations based on the optimized geometries were conducted to confirm the energy minimum of the system (no imaginary frequency) and to obtain the zero-point correction for deriving enthalpies. Atomic point charge distribution was investigated using ChelpG[37] to describe the computational results.

3. RESULTS AND DISCUSSION

3.1. Synthesis of MIL-100(Fe)@PAN. To form a uniform coating of MIL-100(Fe) particles on the electrospun fibers, the organic linker was blended with the pre-spinning solution, presuming that the linker compound from the electrospun fiber surface serves as a nucleation site for MIL-100(Fe) growth (Figure 1a). Afterward, MIL-100(Fe) was grown onto the linker-seeded PAN nanofibers via a hydrothermal process, which accompanies the self-assembly of metals and organic ligands under high pressure and heating conditions. From the SEM and TEM image of MIL-100(Fe)@PAN (Figure 1b,c), a layer of octahedron-shaped MIL-100(Fe) crystals was formed on each strand of fiber. The thickness of the MIL-100(Fe) layer was measured to be ∼95 nm without the noticeable agglomeration of crystals. The average fiber diameter of MIL-100(Fe)@PAN was 342 nm, and the mean size of MIL-100(Fe) crystals was about 71.0 nm (Figure S2). The SEM-EDS (Figure 1d,e) analysis confirms the uniform distribution of the Fe element of MIL-100(Fe) across the composite surface. The FT-IR spectra (Figure S3) and XRD peaks (Figure 1f) indicate the presence of MIL-100(Fe) crystals on the MIL-100(Fe)@PAN web. MIL-100(Fe) powders and the

https://doi.org/10.1021/acsomega.2c01953
ACS Omega 2022, 7, 21145−21155

Table 1. Adsorption Kinetics and Isotherm Parameters Obtained from Linearized Data[a]

model	equation	linear equation	dye	parameters	R^2
pseudo-first order	$Q_t = Q_e\,(1 - e^{-k_1 t})$	$\ln(Q_e - Q_t) = \ln Q_e - k_1 t$	RhB	Q_e = 15.8 mg g^{-1} k_1 = 0.214 min^{-1}	0.990
			MO	Q_e = 11.6 mg g^{-1} k_1 = 0.292 min^{-1}	0.856
pseudo-second order	$Q_t = \frac{k_2 Q_e^2 t}{1 + k_2 Q_e t}$	$\frac{t}{Q_t} = \frac{1}{k_2 Q_e^2} + \frac{1}{Q_e} t$	RhB	Q_e = 19.5 mg g^{-1} k_2 = 0.0125 g mg^{-1} min^{-1}	0.951
			MO	Q_e = 14.9 mg g^{-1} k_2 = 0.0785 mg^{-1} min^{-1}	0.992
Freundlich	$Q_e = k_F C_e^{1/n}$	$\log Q_e = \log k_F + \left(\frac{1}{n}\right)\log C_e$	RhB	k_F = 9.75 n = 1.18	0.988
			MO	k_F = 4.06 n = 0.91	0.967

[a] Q_e and Q_t are the amount of dye adsorbed per gram of MIL-100(Fe)@PAN (mg g^{-1}) at equilibrium and time t, respectively. k_1 and k_2 are the pseudo-first-order (min^{-1}) and pseudo-second-order (g mg^{-1} min^{-1}) rate constants, respectively. C_e is the equilibrium dye concentration in solution (mg L^{-1}). In the Freundlich isotherm model, k_F and n are obtained from fitting the experimental results to the model.

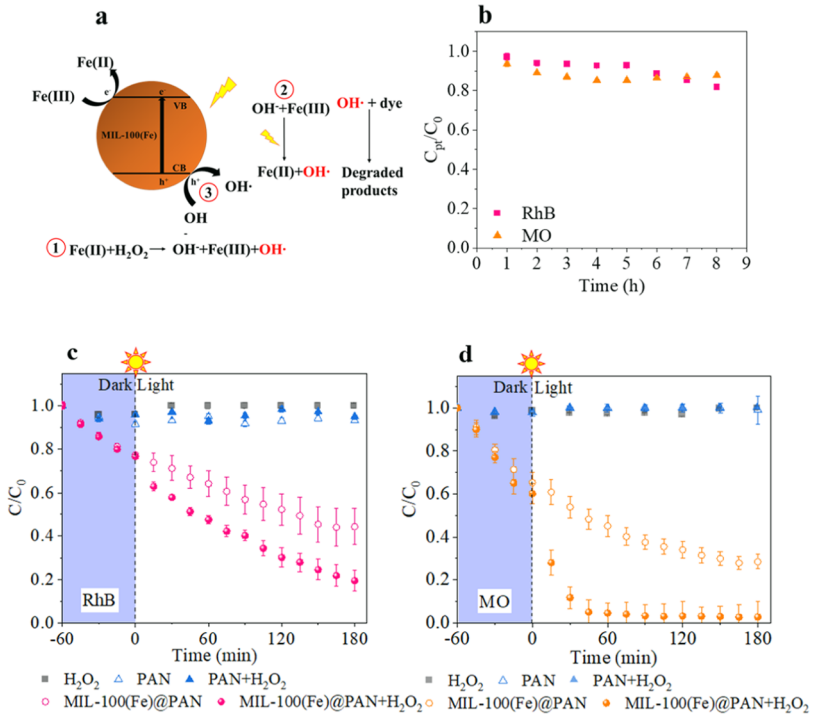

Figure 3. Adsorptive and photocatalytic removal efficiency of RhB and MO under visible light. (a) Illustration of the photo-Fenton reaction of MIL-100(Fe). (b) Photocatalytic degradation after saturation at 20 mg L^{-1}. (c) Photocatalytic degradation of RhB and (d) MO after 60 min of adsorption in the dark.

MIL-100(Fe)@PAN membrane showed characteristic peaks at 3.4, 3.9, 6.3, 10.2, and 11° corresponding to (220), (311), (333), (842), and (422) planes of the MIL-100(Fe).[38−40]

The band gap was measured to be 2.17 eV from the Tauc plot in Figure 1h, and this band gap energy is small enough to be excited under visible light. The mass ratio (%) of MIL-100(Fe) from MIL-100(Fe)@PAN was estimated to be about 60.4% from TGA analysis, and the detailed calculation is shown in SI Section I and Figure S4. The BET N_2 adsorption−desorption isotherms exhibited the typical type IV isotherm with hysteresis, which indicated the presence of both mesopores (2−5 nm) and micropores (up to 2 nm) in MIL-100(Fe) (Figure 1g).[41] The BET surface area of MIL-100(Fe) was measured to be 1357 m^2 g^{-1} with a pore volume of 0.89 cm^3 g^{-1}, and this was in good agreement with the previous report that synthesized MIL-100(Fe) by the solvothermal method.[42,43]

3.2. Adsorption Kinetics and Isotherm of the MIL-100(Fe)@PAN Composite. The adsorption of organic contaminants on MIL-100(Fe)@PAN nanocomposites was investigated, employing a cationic dye, RhB, and an anionic dye, MO, as model contaminants. Figure 2a depicts the adsorbed mass of dyes per unit mass of MIL-100(Fe)@PAN (mg g^{-1}) at the initial dye concentration of 20 mg L^{-1}. MO adsorption occurred more rapidly, and this tendency was consistent for the tests with varied dye concentrations of 10, 15, 20, and 25 mg L^{-1} (Figure S5). More rapid adsorption of MO over RhB is due to the favorable electrostatic interactions between anionic MO dye and MIL-100(Fe). The zeta potential of MIL-100(Fe) was measured to be +3.20 mV in

https://doi.org/10.1021/acsomega.2c01953
ACS Omega 2022, 7, 21145−21155

the aqueous phase at pH 7, implicating that an electrostatic attraction would exist between MIL-100(Fe) and MO under aqueous conditions; as a result, facilitated adsorption occurred for MO over RhB. No such effect is anticipated for the cationic dye, RhB, resulting in slower adsorption than MO. However, the saturation adsorptions (Q_e) of MO and RhB at 20 mg L^{-1} were similar, suggesting that other molecular interactions also play a role in the adsorption process.[44]

The adsorption data were fitted to the pseudo-first-order and the pseudo-second-order kinetic equations in Figure 2b,c, and the kinetic equations with the fitted constants are shown in Table 1. While the experimental data of RhB adsorption were well-fitted with both the pseudo-first- and second-order model ($R^2 \sim 0.990$ and ~0.951), the MO data fitted better with the pseudo-second-order model, allowing an adequate prediction of time-dependent dye adsorption. From the pseudo-second-order model that fits well with both MO and RhB data (Figure 2c), the kinetic constant, k_2 was larger for MO than RhB, indicating a faster adsorption rate of MO over RhB.

In Figure 2d, equilibrium adsorption capacities of MIL-100(Fe)@PAN are shown for dye concentrations of 40, 50, 60, and 70 mg L^{-1}. Regardless of adsorption rates, the maximum adsorption capacity appeared to be similar for both dyes. The functional groups of MIL-100(Fe) may induce various molecular interactions including van der Waals interaction, $\pi-\pi$ interaction, and hydrogen bonding, and such interactions would allow binding of dyes with MIL-100(Fe) with either charges.[45−47] Adsorption isotherm of MIL-100(Fe)@PAN was investigated by fitting the experimental data to the Freundlich model (Figure 2e and Table 1), assuming that the heterogeneous multilayer adsorption would occur on MIL-100(Fe)@PAN. Both RhB and MO adsorptions fitted fairly well with the Freundlich equation as a suitable isotherm model. Based on the linear fittings, the adsorption constants k_F and n are calculated in Table 1. The $1/n$ is commonly regarded as a heterogeneity factor. The value n greater than 1 implies that physical adsorption is favored.[48,49] In this study, RhB shows $n > 1$, indicating the adsorption of RhB is largely dependent on the physical interaction between RhB and MIL-100(Fe)@PAN. For MO, n was less than 1, implying that chemisorption also contributes to the overall adsorption of MO to MIL-100(Fe)@PAN.

3.3. Adsorptive and Photocatalytic Removal of Dyes.

Figure 3a demonstrates the photo-induced Fenton reaction of MIL-100(Fe), in which $^{\bullet}OH$ radicals are produced as the main ROS that participates in the degradation of dyes.[50,51] Compared to other metal-based semiconductors such as zinc oxide (band gap of 3.3 eV) and titanium oxide (band gap of 3.2 eV),[52] MIL-100(Fe) has a lower band gap energy of 2.17 eV, and the photocatalytic reaction can occur under visible light irradiation. Due to a small band gap, the recombination of electrons and hole can occur easily, deterring ROS generation. To inhibit electron−hole recombination, H_2O_2 is added to the reaction as an electron acceptor, and the efficiency of $^{\bullet}OH$ generation is improved.[19] At the same time, H_2O_2 acts as a catalyst for the Fenton reaction, and $^{\bullet}OH$ produced from this reaction initiates photocatalytic decomposition.[20] To examine the dominant radical species that participate in the photodegradation, the photocatalytic efficiency was measured using different radical scavengers, as described in SI Section III and Figure S6. As radical scavengers, isopropanol (IPA), benzoquinone (BQ), and ammonium oxalate (AO) were used to quench $^{\bullet}OH$, $O_2^{\bullet-}$, and holes, respectively. The result in Figure S6 shows that only IPA dramatically reduced the photodegradation performance, confirming that $^{\bullet}OH$ is the dominant ROS species that were involved in the photo-induced Fenton reaction for photodegradation of dyes.

After the complete adsorption of dyes at equilibrium in 20 g mL^{-1}, photocatalytic degradation barely occurred (Figure 3b). It seems that the adsorption sites of MIL-100(Fe) are fully covered by the dye molecules, inhibiting the effective photocatalytic reaction. To observe both the adsorption and photocatalytic effect of MIL-100(Fe)@PAN on the removal of dyes, the test setup was made for the first stage of partial adsorption and the later stage of photocatalytic reaction with concurrent adsorption. In this test, the composite membrane was immersed in the dye solution in the dark for 60 min to induce only adsorption without photocatalytic interference; after 60 min, the visible light (white LED, 20 W) was turned on to proceed the photocatalytic activity (Figure 3c,d). It should be noted that the adsorption did not reach equilibrium until 60 min, and both photocatalysis and adsorption may occur simultaneously after the light is on.

For both RhB and MO, the dye removal efficiency of MIL-100(Fe)@PAN was compared to those of control tests. When H_2O_2 was added to the dye solution without MIL-100(Fe), no significant dye degradation occurred. As the addition of H_2O_2 initiates the photocatalytic reaction, the test of MIL-100(Fe)@PAN with H_2O_2 shows the effect of both adsorptive and photocatalytic degradation after light is on (from time zero). During the first 60 min tested in the dark, only the adsorption would occur for MIL-100(Fe)@PAN; this is confirmed by the result that adsorptions of MIL-100(Fe)@PAN with and without H_2O_2 coincided within 60 min. The discrepancy between MIL-100(Fe)@PAN with and without H_2O_2 is attributed to the photocatalytic activity for the MIL-100(Fe)@PAN + H_2O_2 test. The difference of removal efficiency between MIL-100(Fe)@PAN with and without H_2O_2 evolved larger as photodegradation proceeded. Both adsorption and photocatalytic efficiency appeared to be higher for the MO dye within 240 min of the test period. Of the total RhB removal efficiency in terms of time by the adsorptive and photocatalytic activity (~80%), adsorption contributed ~58%, and the photocatalytic reaction contributed an additional 22% to the removal. For 20 mg L^{-1} MO solution, the adsorption efficiency reached around ~40% for MIL-100(Fe)@PAN in the dark within 60 min. Upon light irradiation from time zero, MIL-100(Fe)@PAN showed steep removal efficiency of MO to about 99% in the presence of H_2O_2. It can be inferred that, once the light was turned on, the photocatalytic degradation became a dominant reaction for MO (from 0 to +60 min), attaining ~99% efficiency. It is notable that the dominant removal mechanism for MO appeared to be photodegradation while MO also showed faster adsorption than RhB during the first 60 min.

The mechanical stability of MIL-100(Fe)@PAN after the concurrent photodegradation and adsorption for 20 mg L^{-1} RhB and MO was further investigated via XRD, FT-IR, and stress−strain behavior in Figures S7−S9, respectively. Both XRD peaks and FT-IR spectra indicate that MIL-100(Fe)@PAN has proper mechanical stability after photodegradation and adsorption in the aqueous solution. The stress−strain curve of the dried MIL-100(Fe)@PAN after photodegradation showed a decrease in both stress and strain after 4 h of the photodegradation process in an aqueous solution. As the experiment proceeded, the dye molecules accumulated on the

https://doi.org/10.1021/acsomega.2c01953
ACS Omega 2022, 7, 21145−21155

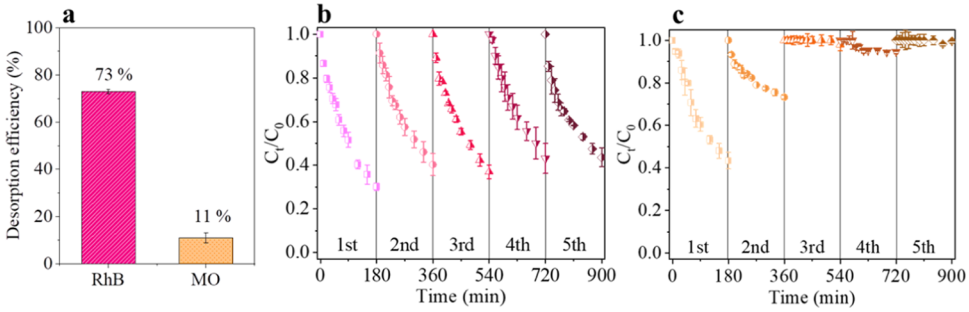

Figure 4. Reusability of MIL-100(Fe)@PAN with RhB and MO. (a) Desorption efficiency of RhB and MO with ethanol cleansing. The repeated cycles of adsorption of 5 mg L^{-1}(b) RhB and (c) MO after desorption.

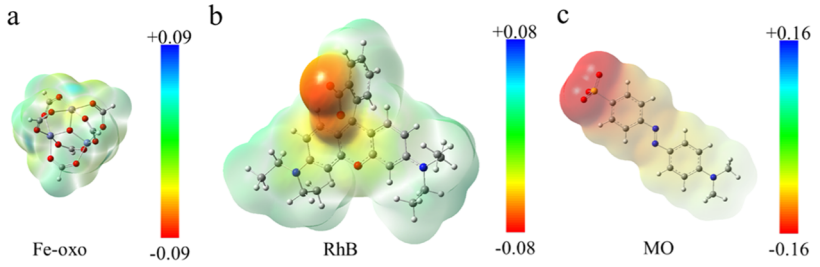

Figure 5. Optimized structures with the distribution of the electrostatic potential by DFT calculation based on the B3LYP/6-311+G(d,p)/LANL2DZ level of theory, the (a) trimeric Fe-oxo cluster model (Fe_3O), (b) RhB zwitterion, and (c) MO (Fe: purple, oxygen: red, carbon: gray, hydrogen: white, nitrogen: blue, sulfur: yellow). Blue and red regions indicate a relatively positive and negative charge distribution, respectively.

surface of the sample, and this led to the decrease of strain. In addition, as the photodegradation proceeded, the generated radicals not only degraded the pollutants but also deteriorated the fiber strength.

3.4. Removal Efficiency with Repeated Use of MIL-100(Fe)@PAN. The dye adsorption efficiency with repeated use of MIL-100(Fe)@PAN was tested at a dye concentration of 5 mg L^{-1} (Figure 4b,c). After every adsorption test, the adsorbed RhB and MO on the composite membranes were washed with ethanol to regenerate the available adsorptive sites. The desorption efficiencies were measured to be about 75% for RhB and 11% for MO after ethanol washing (Figure 4a). The negligible desorption on MO may be attributed to strong electrostatic adsorption of MO to MIL-100(Fe)@PAN, as is supported by the DFT calculation presented in the later section. Accordingly, the repeated adsorption of MO remained minimal as almost full adsorption was attained in the first cycle. On the other hand, RhB maintained an adsorption efficiency of 60−70% with the repeated adsorption tests; the loss in adsorption efficiency was <10% throughout the repeated cycles. The higher desorption efficiency of RhB is probably due to the weaker interaction of physisorption between RhB and MIL-100(Fe)@PAN. RhB molecules were easily detached from the adsorbent by the washing process, and the adsorption efficiency of RhB recovered after washing, giving high resorption efficiencies.

3.5. DFT Analysis. The binding energy between RhB/MO and MIL-100(Fe) was calculated via DFT to elucidate the reusability of the membrane depending on the adsorption/desorption. In Figure 5, a simplified cluster model consisting of 3 Fe atoms capped with 3 formate groups (instead of the original benzene groups) was considered to reduce computational time and cost. This trimeric Fe-oxo node as a building unit of MIL-100(Fe) was previously used to carry out several theoretical studies for MOF adsorption.[53−57] The low- ($2S + 1 = 1$) and high spin states ($2S + 1 = 15$) of the molecule were calculated, showing the ground-state energy in the high spin state (energy gap). Vitillo et al.[55] investigated spin configurations of the cluster model, in which the antiferromagnetic coupling between two Fe centers shows lower energy by only 20 kJ mol^{-1} than the high spin ferromagnetic configuration. Other studies using similar trimetallic building blocks also reported that the energy of antiparallel spin states showed slightly lower or almost no difference compared to that of parallel spin states.[53,57] In addition, the broken-symmetry solution usually faces convergence issues and spin contamination,[53] and has physically improper spin densities.[58] Therefore, the ferromagnetically coupled-cluster model ($2S + 1 = 15$) of MIL-100(Fe) was calculated in this study.

Several researchers have reported the potential structures of RhB in aqueous solution under synthesis conditions,[59−62] whereas MO is known to ionize ($SO_3^- + Na^+$) and exist in negatively charged forms in solutions.[63] Chi et al.[62] reported the optimized molecular structures and the relative Gibbs free energy of the zwitterion and cation of RhB in water and demonstrated that the cations were more stable forms than the zwitterion. In our study, the binding energies of both structures of RhB with MIL-100(Fe) were calculated.

First, DFT calculations were conducted to optimize the ground-state structures of three geometries: trimeric Fe cluster, RhB, and MO. From the optimized geometries, the electrostatic potential (ChelpG population analysis) was derived on each molecule to confirm the more reactive site (Figure 5). Three Fe atoms have relatively positive charges (blue) compared to adjacent areas (Figure 5a) while the oxygen atoms in RhB and MO show strong electronegativity (red). These distributions of electrostatic potential would result in a Coulombic interaction between Fe atoms of Fe_3O and O atoms of RhB/MO (atomic charge of the O atom: −0.55 in RhB and −0.74 in MO).

https://doi.org/10.1021/acsomega.2c01953
ACS Omega 2022, 7, 21145−21155

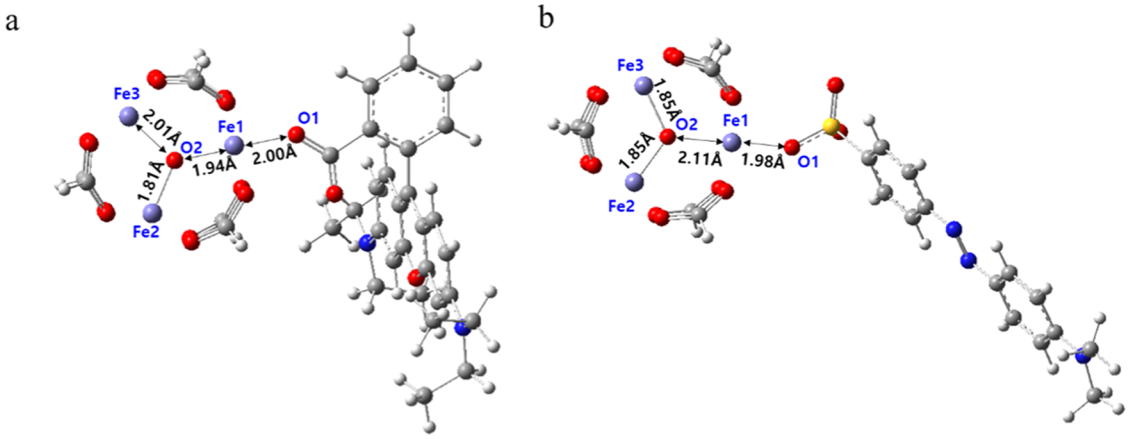

Figure 6. Bond lengths for the ground-state structures of the complex systems: the model cluster with the (a) RhB zwitterion and (b) MO (Fe: purple, oxygen: red, carbon: gray, hydrogen: white, nitrogen: blue, sulfur: yellow).

Based on the above results, the initial geometries for the MIL-100(Fe) MOF and dye complex were established assuming Fe (MOF)−O (dye) interaction. The complexes of the model cluster with RhB and MO were fully optimized at the same level of theory (Figure 6). All optimized geometries were verified by frequency calculations (no imaginary frequency). The bond length of Fe1−O1 (1.98 Å) of the Fe_3O and MO complexes is slightly shorter than that of the model cluster and RhB complex (2.00 Å). The bond length of O2 (the center atom of Fe_3O) and Fe1 in isolated Fe_3O is 1.84 Å, and it slightly increases in both complex molecules as shown in Figure 6 (Fe_3O−RhB: 1.84 Å → 1.94 Å, Fe_3O−MO: 1.84 Å → 2.11 Å). The longer Fe1−O2 distance of the Fe_3O−MO complex (2.11 Å) than that of the Fe_3O−RhB complex (1.94 Å) means stronger interaction between Fe1 and O1 in the Fe_3O−MO complex. The binding energies of Fe_3O−RhB and Fe_3O−MO complexes qualitatively show the bond strength of the Fe−O interaction (Table 2). The binding energy of Fe_3O with the MO anion was larger (−128.6 kJ mol^{-1}) than that of Fe_3O with RhB (−67.7 kJ mol^{-1}). The RhB cation yields a relatively stronger interaction with the model cluster than the neutral RhB (lactone or zwitterion), but still has ∼32 kJ mol^{-1} lower binding energy than the Fe_3O−MO anion complex.

Table 2. Charge, Spin Multiplicity ($2S + 1$), Binding Energy (ΔH) for the Model Cluster (Fe_3O), and Dyes (RhB Cation, RhB, and MO Anion)

molecules	charge	$2S + 1$	ΔH (kJ mol^{-1})[a]
Fe_3O−RhB cation	+1 au	15	−96.5
Fe_3O−RhB	neutral	15	−67.7
Fe_3O−MO anion	−1 au	15	−128.6

[a]Binding energy at 298 K.

It is also possible that the steric hindrance is responsible for the difference in molecular interactions between MIL-100(Fe) and dyes; RhB had a large molecular volume (440.5 $Å^3$, van der Waals volume by Connolly surface analysis using Materials Studio 2016 software) compared to MO (263.0 $Å^3$). Thus, it would be more difficult for RhB to enter the pore openings of MIL-100(Fe) and to interact with the Fe sites inside the pores. As a result, it is likely that RhB, weakly adhering to the MOF surface, is easily detached by the washing process. This result is consistent with our experimental result, in which MO showed stronger interaction with the Fe atom than RhB. As it is more difficult for MO to be detached after adsorption, MO showed poor resorption ability with repeated adsorption tests.

4. CONCLUSIONS

The visible light-induced photocatalytic adsorbent was fabricated by growing MIL-100(Fe) MOF crystals onto the electrospun polyacrylonitrile (PAN) nanofibers, and its purification capability of water-soluble organic foulants was investigated employing an anionic dye, methyl orange (MO) and a cationic dye, rhodamine B (RhB). The experimental adsorption results were fitted with the pseudo-second-order adsorption kinetics, and the rate constants demonstrated that the anionic MO dye was more rapidly adsorbed onto the MIL-100(Fe) grown membrane (MIL-100(Fe)@PAN) than cationic RhB. As MIL-100(Fe) is positively charged in the aqueous phase, electrostatic interactions with dye molecules affected the adsorption rate. Regardless of different adsorption rates, the maximum adsorption capacity of RhB and MO at equilibrium appeared to be similar as adsorption occurred in multilayers following the Freundlich adsorption isotherm. The photocatalytic activity of the membrane was demonstrated under visible light, and the concurrent action of photodegradation and adsorption facilitated the purification process of contaminated water.

The reusability of MIL-100(Fe)@PAN as an adsorbent was investigated by the cyclic adsorption−desorption experiments. The desorption of adsorbed dye molecules was limited for MO, due to the strong interaction between the anionic MO molecule and MIL-100(Fe). The charging effect and the resulting stronger binding energy of MO over RhB were corroborated by DFT analysis. Also, DFT calculations demonstrated the possible volume effect on adsorption/desorption; the size of RhB is larger than the MO molecule, and RhB may have steric hindrance to entering the MOF pores, being weakly adhered onto the MOF surface. As a result, it is likely that RhB is more easily detached from the surface, showing efficient resorption ability. The emphasis of this study lies in the combined investigation of the experimental approach and DFT calculation for a fundamental understanding of the interaction between foulants and MIL-100(Fe)@PAN in the purification process. This study intends to provide informative data on the contribution of adsorption and photocatalytic activity in the simultaneous purification process,

https://doi.org/10.1021/acsomega.2c01953
ACS Omega 2022, 7, 21145−21155

and to give a fundamental understanding of the atomic level interaction of the MIL-100(Fe) adsorbent with the adsorbates with different charges and sizes. This work gives an appreciable example devoted to the development of highly efficient photocatalytic adsorbents for wastewater purification.

■ ASSOCIATED CONTENT

Supporting Information

The Supporting Information is available free of charge at https://pubs.acs.org/doi/10.1021/acsomega.2c01953.

Characterization of MIL-100(Fe)@PAN (Section I); viscosity and shear stress versus shear rate of the pre-spinning solution 10 wt % PAN/DMF with the added precursor (Figure S1); size distribution of (a) the diameter of MIL-100(Fe)@PAN and (b) MIL-100(Fe) particles (Figure S2); FT-IR spectrum of H_3BTC, MIL-100(Fe), MIL-100(Fe)@PAN, and PAN (Figure S3); TGA analysis of PAN, MIL-100(Fe), and MIL-100(Fe) @PAN (Figure S4); adsorption performance of MIL-100(Fe)@PAN for rhodamine B (RhB) and methyl orange (MO) (Section II); MIL-100(Fe)@PAN adsorption for RhB and MO at concentrations of (a) 10 mg L^{-1}, (b) 15 mg L^{-1}, and (C) 25 mg L^{-1}, respectively; scavenger effect on the photodegradation process of MIL-100(Fe)@PAN (Section III); effect of scavengers (IPA, BQ, and AO) on the photodegradation process (Figure S6); characterization of MIL-100(Fe)@PAN after simultaneous photodegradation and adsorption (Section IV); XRD peaks of MIL-100(Fe)@PAN before use and after simultaneous photodegradation and adsorption of RhB and MO (Figure S7); FT-IR spectrum of MIL-100(Fe)@PAN after simultaneous photodegradation and adsorption of RhB and MO (Figure S8); and stress−strain curves of MIL-100(Fe)@PAN after simultaneous photodegradation and adsorption of RhB and MO for 4 h (Figure S9) (PDF)

■ AUTHOR INFORMATION

Corresponding Author

Jooyoun Kim − *Department of Textiles, Merchandising and Fashion Design, Seoul National University, Seoul 08826, Republic of Korea; Research Institute of Human Ecology, Seoul National University, Seoul 08826, Republic of Korea;* orcid.org/0000-0001-5043-9378; Email: jkim256@snu.ac.kr

Authors

Halim Lee − *Department of Textiles, Merchandising and Fashion Design, Seoul National University, Seoul 08826, Republic of Korea;* orcid.org/0000-0003-4229-9699

Hyungwoo Lee − *Institute of Advanced Machines and Design and Division of Multiscale Mechanical Design, School of Mechanical and Aerospace Engineering, Seoul National University, Seoul 08826, Republic of Korea*

Soyeon Ahn − *Department of Textiles, Merchandising and Fashion Design, Seoul National University, Seoul 08826, Republic of Korea;* orcid.org/0000-0001-8997-9873

Complete contact information is available at: https://pubs.acs.org/10.1021/acsomega.2c01953

Author Contributions

The manuscript was written through contributions of all authors. All authors have given approval to the final version of the manuscript.

Notes

The authors declare no competing financial interest.

■ ACKNOWLEDGMENTS

This work was supported by the National Research Foundation of Korea (NRF) grant funded by the Korea government (MSIT) (No. 2022R1A2C2003072).

■ REFERENCES

(1) Rojas, S.; Horcajada, P. Metal−Organic Frameworks for the Removal of Emerging Organic Contaminants in Water. *Chem. Rev.* **2020**, *120*, 8378−8415.

(2) de Andrade, J. R.; Oliveira, M. F.; da Silva, M. G. C.; Vieira, M. G. A. Adsorption of Pharmaceuticals from Water and Wastewater Using Nonconventional Low-Cost Materials: A Review. *Ind. Eng. Chem. Res.* **2018**, *57*, 3103−3127.

(3) Azhar, M. R.; Arafat, Y.; Zhong, Y.; Khiadani, M.; Tade, M. O.; Wang, S.; Shao, Z. An Adsorption−Catalysis Pathway toward Sustainable Application of Mesoporous Carbon Nanospheres for Efficient Environmental Remediation. *ACS EST Water* **2021**, *1*, 145−156.

(4) Luo, J.; Fu, K.; Yu, D.; Hristovski, K. D.; Westerhoff, P.; Crittenden, J. C. Review of Advances in Engineering Nanomaterial Adsorbents for Metal Removal and Recovery from Water: Synthesis and Microstructure Impacts. *ACS EST Eng.* **2021**, *1*, 623−661.

(5) Loeb, S. K.; Alvarez, P. J. J.; Brame, J. A.; Cates, E. L.; Choi, W.; Crittenden, J.; Dionysiou, D. D.; Li, Q.; Li-Puma, G.; Quan, X.; Sedlak, D. L.; David Waite, T.; Westerhoff, P.; Kim, J.-H. The Technology Horizon for Photocatalytic Water Treatment: Sunrise or Sunset? *Environ. Sci. Technol.* **2019**, *53*, 2937−2947.

(6) Guo, Q.; Zhou, C.; Ma, Z.; Yang, X. Fundamentals of TiO_2 Photocatalysis: Concepts, Mechanisms, and Challenges. *Adv. Mater.* **2019**, *31*, No. 1901997.

(7) Mirzaeifard, Z.; Shariatinia, Z.; Jourshabani, M.; Rezaei Darvishi, S. M. ZnO Photocatalyst Revisited: Effective Photocatalytic Degradation of Emerging Contaminants Using S-Doped ZnO Nanoparticles under Visible Light Radiation. *Ind. Eng. Chem. Res.* **2020**, *59*, 15894−15911.

(8) Fazal, T.; Razzaq, A.; Javed, F.; Hafeez, A.; Rashid, N.; Amjad, U. S.; Rehman, M. S. U.; Faisal, A.; Rehman, F. Integrating Adsorption and Photocatalysis: A Cost Effective Strategy for Textile Wastewater Treatment Using Hybrid Biochar-TiO_2 Composite. *J. Hazard. Mater.* **2020**, *390*, No. 121623.

(9) Wang, Q.; Gao, Q.; Al-Enizi, A. M.; Nafady, A.; Ma, S. Recent Advances in MOF-Based Photocatalysis: Environmental Remediation Under Visible Light. *Inorg. Chem. Front.* **2020**, *7*, 300−339.

(10) Parmar, B.; Bisht, K. K.; Rajput, G.; Suresh, E. Recent Advances in Metal−Organic Frameworks as Adsorbent Materials for Hazardous Dye Molecules. *Dalton Trans.* **2021**, *50*, 3083−3108.

(11) Li, X.; Wang, B.; Cao, Y.; Zhao, S.; Wang, H.; Feng, X.; Zhou, J.; Ma, X. Water Contaminant Elimination Based on Metal−Organic Frameworks and Perspective on Their Industrial Applications. *ACS Sustainable Chem. Eng.* **2019**, *7*, 4548−4563.

(12) Kampouri, S.; Nguyen, T. N.; Spodaryk, M.; Palgrave, R. G.; Züttel, A.; Smit, B.; Stylianou, K. C. Concurrent Photocatalytic Hydrogen Generation and Dye Degradation Using MIL-125-NH_2 under Visible Light Irradiation. *Adv. Funct. Mater.* **2018**, *28*, No. 1806368.

(13) Seo, J. Y.; Song, Y.; Lee, J.-H.; Kim, H.; Cho, S.; Baek, K.-Y. Robust Nanocellulose/Metal−Organic Framework Aerogel Composites: Superior Performance for Static and Continuous Disposal of Chemical Warfare Agent Simulants. *ACS Appl. Mater. Interfaces* **2021**, *13*, 33516−33523.

(14) Liu, X.; Zhou, Y.; Zhang, J.; Tang, L.; Luo, L.; Zeng, G. Iron Containing Metal−Organic Frameworks: Structure, Synthesis, and Applications in Environmental Remediation. *ACS Appl. Mater. Interfaces* **2017**, *9*, 20255−20275.
(15) Yang, J.; Li, J.; Yan, X.; Lyu, Y.; Xing, N.; Yang, P.; Song, P.; Zuo, M. Three-Dimensional Hierarchical HRP-MIL-100(Fe)@ TiO2@Fe3O4 Janus Magnetic Micromotor as a Smart Active Platform for Detection and Degradation of Hydroquinone. *ACS Appl. Mater. Interfaces* **2022**, *14*, 6484−6498.
(16) Zhang, S.; Zhang, Y.; Baig, F.; Liu, T.-F. Synthesis and Applications of Stable Iron-Based Metal−Organic Framework Materials. *Cryst. Growth Des.* **2021**, *21*, 3100−3122.
(17) Wang, S.; Serre, C.; et al. Toward Green Production of Water-Stable Metal−Organic Frameworks Based on High-Valence Metals with Low Toxicities. *ACS Sustainable Chem. Eng.* **2019**, *7*, 11911−11927.
(18) He, X.; Fang, H.; Gosztola, D. J.; Jiang, Z.; Jena, P.; Wang, W.-N. Mechanistic Insight into Photocatalytic Pathways of MIL-100(Fe)/TiO_2 Composites. *ACS Appl. Mater. Interfaces* **2019**, *11*, 12516−12524.
(19) da Silva, A. C.; Almeida, M. R.; Rodriguez, M.; Machado, A. R. T.; de Oliveira, L. C. A.; Pereira, M. C. Improved Photocatalytic Activity of δ-FeOOH by Using H_2O_2 as an Electron Acceptor. *J. Photochem. Photobiol. A: Chem.* **2017**, *332*, 54−59.
(20) Ai, L.; Zhang, C.; Li, L.; Jiang, J. Iron Terephthalate Metal−Organic Framework: Revealing the Effective Activation of Hydrogen Peroxide for the Degradation of Organic Dye Under Visible Light Irradiation. *Appl. Catal., B* **2014**, *148−149*, 191−200.
(21) Lee, J.; Jung, S.; Park, H.; Kim, J. Bifunctional ZIF-8 Grown Webs for Advanced Filtration of Particulate and Gaseous Matters: Effect of Charging Process on the Electrostatic Capture of Nanoparticles and Sulfur Dioxide. *ACS Appl. Mater. Interfaces* **2021**, *13*, 50401−50410.
(22) de Koning, M. C.; Ma, K.; van Grol, M.; Iordanov, I.; Kruijne, M. J. L.; Idrees, K. B.; Xie, H.; Islamoglu, T.; Bross, R. P. T.; Farha, O. K. Development of a Metal−Organic Framework/Textile Composite for the Rapid Degradation and Sensitive Detection of the Nerve Agent VX. *Chem. Mater* **2022**, *34*, 1269−1277.
(23) Li, P.; Li, J.; Feng, X.; Li, J.; Hao, Y.; Zhang, J.; Wang, H.; Yin, A.; Zhou, J.; Ma, X.; Wang, B. Metal-Organic Frameworks with Photocatalytic Bactericidal Activity for Integrated Air Cleaning. *Nat. Commun.* **2019**, *10*, No. 2177.
(24) Yan, H.; Liu, L.; Wang, R.; Zhu, W.; Ren, X.; Luo, L.; Zhang, X.; Luo, S.; Ai, X.; Wang, J. Binary Composite MoS_2/TiO_2 Nanotube Arrays as a Recyclable and Efficient Photocatalyst for Solar Water Disinfection. *Chem. Eng. J.* **2020**, *401*, No. 126052.
(25) Li, P.-X.; Yan, X.-Y.; Song, X.-M.; Li, J.-J.; Ren, B.-H.; Gao, S.-Y.; Cao, R. Zirconium-Based Metal−Organic Framework Particle Films for Visible-Light-Driven Efficient Photoreduction of CO_2. *ACS Sustainable Chem. Eng.* **2021**, *9*, 2319−2325.
(26) Zhu, Z.-H.; Liu, Y.; Song, C.; Hu, Y.; Feng, G.; Tang, B. Z. Porphyrin-Based Two-Dimensional Layered Metal−Organic Framework with Sono-/Photocatalytic Activity for Water Decontamination. *ACS Nano* **2022**, *16*, 1346−1357.
(27) Hang, M.-T.; Cheng, Y.; Wang, Y.-T.; Li, H.; Zheng, M.-Q.; He, M.-Y.; Chen, Q.; Zhang, Z.-H. Rational Synthesis of Isomorphic Rare Earth Metal−Organic Framework Materials for Simultaneous Adsorption and Photocatalytic Degradation of Organic Dyes in Water. *CrystEngComm.* **2022**, *24*, 552−559.
(28) Abd El Khalk, A. A.; Betiha, M. A.; Mansour, A. S.; Abd El Wahed, M. G.; Al-Sabagh, A. M. High Degradation of Methylene Blue Using a New Nanocomposite Based on Zeolitic Imidazolate Framework-8. *ACS Omega* **2021**, *6*, 26210−26220.
(29) Wang, Z.; Miao, R.; He, L.; Guan, Q.; Shi, Y. Green Synthesis of MIL-100 (Fe) Derivatives and Revealing Their Structure-Activity Relationship for 2, 4-Dichlorophenol Photodegradation. *Chemosphere* **2022**, *291*, No. 132950.
(30) Zhou, W.; Zhang, Y.-y.; Shi, Y.-d. In Situ Loading TiO_2 and Its Photocatalysis and UV Resistance on Cotton Fabric. *Fibers Polym.* **2017**, *18*, 1073−1078.
(31) Frisch, M.; Trucks, G.; Schlegel, H.; Scuseria, G.; Robb, M.; Cheeseman, J.; Scalmani, G.; Barone, V.; Mennucci, B.; Petersson, G.et al.*Gaussian 09*, revision D. 01; Gaussian Inc.: Wallingford CT, 2009.
(32) Becke, A. D. Density-Functional Thermochemistry. III. The Role of Exact Exchange. *J. Chem. Phys.* **1993**, *98*, 5648−5652.
(33) Lee, C.; Yang, W.; Parr, R. G. Development of the Colle-Salvetti Correlation-Energy Formula into a Functional of the Electron Density. *Phys. Rev. B* **1988**, *37*, 785.
(34) Curtiss, L. A.; McGrath, M. P.; Blaudeau, J. P.; Davis, N. E.; Binning, R. C., Jr.; Radom, L. Extension of Gaussian-2 Theory to Molecules Containing Third-Row Atoms Ga−Kr. *J. Chem. Phys.* **1995**, *103*, 6104−6113.
(35) Giordan, M.; Custodio, R. Basis Set Modeling for Molecular Calculations Using Effective Core Potential. *J. Comput. Chem.* **1997**, *18*, 1918−1929.
(36) DeFrees, D. J.; McLean, A. Molecular Orbital Predictions of the Vibrational Frequencies of Some Molecular Ions. *J. Chem. Phys.* **1985**, *82*, 333−341.
(37) Breneman, C. M.; Wiberg, K. B. Determining Atom-Centered Monopoles from Molecular Electrostatic Potentials. The Need for High Sampling Density in Formamide Conformational Analysis. *J. Comput. Chem.* **1990**, *11*, 361−373.
(38) Horcajada, P.; Surblé, S.; Serre, C.; Hong, D.-Y.; Seo, Y.-K.; Chang, J.-S.; Grenèche, J.-M.; Margiolaki, I.; Férey, G. Synthesis and Catalytic Properties of MIL-100 (Fe), an Iron (III) Carboxylate with Large Pores. *Chem. Commun.* **2007**, *27*, 2820−2822.
(39) Mohammadifard, Z.; Saboori, R.; Mirbagheri, N. S.; Sabbaghi, S. Heterogeneous Photo-Fenton Degradation of Formaldehyde Using MIL-100 (Fe) Under Visible Light Irradiation. *Environ. Pollut.* **2019**, *251*, 783−791.
(40) Dung, N. T.; Hue, T. T.; Thao, V. D.; Huy, N. N. Preparation of Mn_2O_3/MIL-100 (Fe) Composite and Its Mechanism for Enhancing the Photocatalytic Removal of Rhodamine B in Water. *RSC Adv.* **2021**, *11*, 28496−28507.
(41) Schneider, P. Adsorption Isotherms of Microporous-Mesoporous Solids Revisited. *Appl. Catal., A* **1995**, *129*, 157−165.
(42) Yang, J.; Niu, X.; An, S.; Chen, W.; Wang, J.; Liu, W. Facile Synthesis of Bi_2MoO_6−MIL-100 (Fe) Metal−Organic Framework Composites with Enhanced Photocatalytic Performance. *RSC Adv.* **2017**, *7*, 2943−2952.
(43) Nivetha, R.; Gothandapani, K.; Raghavan, V.; Jacob, G.; Sellappan, R.; Bhardwaj, P.; Pitchaimuthu, S.; Kannan, A. N. M.; Jeong, S. K.; Grace, A. N. Highly Porous MIL-100 (Fe) for the Hydrogen Evolution Reaction (HER) in Acidic and Basic Media. *ACS Omega* **2020**, *5*, 18941−18949.
(44) Jia, Y.; Jin, Q.; Li, Y.; Sun, Y.; Huo, J.; Zhao, X. Investigation of the Adsorption Behaviour of Different Types of Dyes on MIL-100 (Fe) and Their Removal from Natural Water. *Anal. Methods* **2015**, *7*, 1463−1470.
(45) Guo, X.-Z.; Han, S.-S.; Yang, J.-M.; Wang, X.-M.; Chen, S.-S.; Quan, S. Effect of Synergistic Interplay between Surface Charge, Crystalline Defects, and Pore Volume of MIL-100 (Fe) on Adsorption of Aqueous Organic Dyes. *Ind. Eng. Chem. Res.* **2020**, *59*, 2113−2122.
(46) Xu, Q.; Zhao, X. Electrostatic Interactions versus van der Waals Interactions in the Self-Assembly of Dispersed Nanodiamonds. *J. Mater. Chem.* **2012**, *22*, 16416−16421.
(47) Shahnawaz Khan, M.; Khalid, M.; Shahid, M. What Triggers Dye Adsorption by Metal Organic Frameworks? The Current Perspectives. *Mater. Adv.* **2020**, *1*, 1575−1601.
(48) Crini, G.; Peindy, H. N.; Gimbert, F.; Robert, C. Removal of CI Basic Green 4 (Malachite Green) from Aqueous Solutions by Adsorption Using Cyclodextrin-Based Adsorbent: Kinetic and Equilibrium Studies. *Sep. Purif. Technol.* **2007**, *53*, 97−110.

https://doi.org/10.1021/acsomega.2c01953
ACS Omega 2022, 7, 21145−21155

(49) El Nemr, A.; Khaled, A.; Abdelwahab, O.; El-Sikaily, A. Treatment of Wastewater Containing Toxic Chromium Using New Activated Carbon Developed from Date Palm Seed. *J. Hazard. Mater.* **2008**, *152*, 263−275.
(50) He, Y.; Dong, W.; Li, X.; Wang, D.; Yang, Q.; Deng, P.; Huang, J. Modified MIL-100 (Fe) for Enhanced Photocatalytic Degradation of Tetracycline Under Visible-Light Irradiation. *J. Colloid Interface Sci.* **2020**, *574*, 364−376.
(51) Lim, H.; Namkung, K. C.; Yoon, J. Theoretical Understanding of Fenton Chemistry. *Appl. Chem. Eng.* **2005**, *16*, 9−14.
(52) Ritacco, I.; Sacco, O.; Caporaso, L.; Camellone, M. F. DFT Investigation of Substitutional and Interstitial Nitrogen-Doping Effects on a ZnO(100)−TiO_2(101) Heterojunction. *J. Phys. Chem. C* **2022**, *126*, 3180−3193.
(53) Mavrandonakis, A.; Vogiatzis, K. D.; Boese, A. D.; Fink, K.; Heine, T.; Klopper, W. Ab initio Study of the Adsorption of Small Molecules on Metal−Organic Frameworks with oxo-Centered Trimetallic Building Units: The Role of the Undercoordinated Metal Ion. *Inorg. Chem.* **2015**, *54*, 8251−8263.
(54) Chen, Y.-R.; Liou, K.-H.; Kang, D.-Y.; Chen, J.-J.; Lin, L.-C. Investigation of the Water Adsorption Properties and Structural Stability of MIL-100 (Fe) with Different Anions. *Langmuir* **2018**, *34*, 4180−4187.
(55) Vitillo, J. G.; Bhan, A.; Cramer, C. J.; Lu, C. C.; Gagliardi, L. Quantum Chemical Characterization of Structural Single Fe (II) Sites in MIL-type Metal−Organic Frameworks for the Oxidation of Mmethane to Methanol and Ethane to Ethanol. *ACS Catal.* **2019**, *9*, 2870−2879.
(56) Simons, M. C.; Vitillo, J. G.; Babucci, M.; Hoffman, A. S.; Boubnov, A.; Beauvais, M. L.; Chen, Z.; Cramer, C. J.; Chapman, K. W.; Bare, S. R.; et al. Structure, Dynamics, and Reactivity for Light Alkane Oxidation of Fe (II) Sites Situated in the Nodes of a Metal−Organic Framework. *J. Am. Chem. Soc.* **2019**, *141*, 18142−18151.
(57) Mileo, P. G. M.; Ho Cho, K.; Park, J.; Devautour-Vinot, S.; Chang, J.-S.; Maurin, G. Unraveling the Water Adsorption Mechanism in the Mesoporous MIL-100 (Fe) Metal−Organic Framework. *J. Phys. Chem. C* **2019**, *123*, 23014−23025.
(58) Cramer, C. J.; Truhlar, D. G. Density Functional Theory for Transition Metals and Transition Metal Chemistry. *Phys. Chem. Chem. Phys.* **2009**, *11*, 10757−10816.
(59) Zhao, W.; Li, B.; Xu, S.; Zhao, Q. DFT/TD-DFT Study of the Structural and Spectral Properties of Two Forms of Rhodamine B. *J. Theor. Comput. Chem.* **2015**, *14*, No. 1550030.
(60) Setiawan, D.; Kazaryan, A.; Martoprawiro, M. A.; Filatov, M. A First Principles Study of Fluorescence Quenching in Rhodamine B Dimers: How Can Quenching Occur in Dimeric Species? *Phys. Chem. Chem. Phys.* **2010**, *12*, 11238−11244.
(61) Goto, Y.; Nema, Y.; Matsuoka, K. Removal of Zwitterionic Rhodamine B Using Foam Separation. *J. Oleo Sci.* **2020**, *69*, 563−567.
(62) Chi, W.; Qi, Q.; Lee, R.; Xu, Z.; Liu, X. A Unified Push−Pull Model for Understanding the Ring-Opening Mechanism of Rhodamine Dyes. *J. Phys. Chem. C* **2020**, *124*, 3793−3801.
(63) Akama, Y.; Tong, A.; Ito, M.; Tanaka, S. The Study of the Partitioning Mechanism of Methyl Orange in an Aqueous Two-Phase System. *Talanta* **1999**, *48*, 1133−1137.

https://doi.org/10.1021/acsomega.2c01953
ACS Omega 2022, 7, 21145−21155